

## Research Paper

## Slit structures: Fundamental mechanisms of mechanical trapping of granular flows



G.R. Goodwin, C.E. Choi\*

Department of Civil Engineering, The University of Hong Kong, Pokfulam, Hong Kong Special Administrative Region

## ARTICLE INFO

**Keywords:**  
 Landslides  
 Steep creek hazards  
 Granular flows  
 Discrete element method

## ABSTRACT

Slit-structures are rigid structures with one or more slits. To retard steep-creek hazards, slit-structures are sometimes installed to reduce the peak discharge, as well as to mechanically trap grains for frictional flows. However, designs are empirical. It is not possible to assess whether boulders will be trapped, or if smaller discharge of harmless flow material can pass downstream. This study starts by reviewing the inherent difficulties of characterising mechanical trapping processes for granular flows. A calibrated Discrete Element Method (DEM) model is then used to conduct a parametric study of the number of slits, the slit spacing, the Froude number and the ratio between grain and slit size. Results from the DEM study allow three interaction regions to be identified: 'self-cleaning', 'unstable' and 'trapping'. These regimes are extremely sensitive to the slit number, width and spacing, as well as the Froude number. This study shows that existing recommendations may coincide with the unstable region. However, the unstable region should be avoided because of unpredictable trapping behaviour. Additionally, increasing the slit spacing can increase material trapping because of an increase in the duration of binary grain contacts. This increase in the slit spacing tends to prevent shear transmission from slit to slit. Narrowly-spaced double slits may be most effective at the controlling outflow rate whilst enabling 'self-cleaning'.

## 1. Introduction

Mountainous regions are imperilled by landslide-like hazards [1–6]. Slit-structures, such as open check-dams [7–10] (Fig. 1a and b), may be installed in flow paths to regulate discharge. Such structures are typically rigid and have one or more openings. They can both reduce the peak flow rate and trap granular material. The extent of flow-rate regulation and trapping depends heavily on the properties of the flow and the design of the slit. There are two types of trapping: (i) hydraulic and (ii) mechanical.

Hydraulic trapping is exclusive to inviscid flows [11]: slit-structures are designed to cause the upstream Froude number [11–15] to become subcritical. Grains within the flow, which are denser than water, are then able to settle behind the barrier. By contrast, mechanical trapping can occur for both inviscid [10] and frictional [16] flows. If the slits (width  $s$ ) are narrow compared to the flow grain diameter ( $\delta$ ), grains may also become trapped [10] via the formation of arches [16,17]. Trapping [18] can be especially helpful for slit-structures which form part of a multi-barrier network [19], enabling the design requirements of barriers downstream to be reduced [20].

The mechanism of trapping depends on the dominant type of stress within flows, specifically whether flows are inviscid or frictional, as

described using the friction number [21]:

$$N_{\text{fric}} = \frac{\nu_s}{1 - \nu_s} \cdot \frac{(\rho_s - \rho_f)gh}{\dot{\gamma}\mu} \quad (1)$$

where  $\nu_s$  is the solid volume fraction;  $\rho_s$  and  $\rho_f$  are the solid and fluid densities, respectively;  $g$  is acceleration due to the Earth's gravity;  $h$  is the flow depth;  $\dot{\gamma}$  is the shear rate; and  $\mu$  is the dynamic fluid viscosity.  $N_{\text{fric}} < 2000$  corresponds to inviscid flows, whilst  $N_{\text{fric}} > 2000$  indicates dominance of frictional stresses [21].

Whilst a clear theoretical basis exists for designing the slit sizes for hydraulically trapping grains from inviscid flows (e.g. [11,22]), the same cannot be said of mechanical trapping. There are several difficulties in quantitatively dealing with mechanical trapping:

- (i) For the range of  $s/\delta$  for which trapping may occur, interaction between flows and slit-structures is inherently unsteady [10].
- (ii) The dependence of interaction dynamics on the grain diameter ( $\delta$ ) [16] implies that macroscopic flow properties cannot be relied on to describe either the flow rate or trapping. This problem is compounded by the wide range of grain sizes present within geophysical flows [23,24]. Additionally, stable arch formation [25–28] is

\* Corresponding author.

E-mail addresses: [grrgoodwin@connect.ust.hk](mailto:grrgoodwin@connect.ust.hk) (G.R. Goodwin), [cechoi@hku.hk](mailto:cechoi@hku.hk) (C.E. Choi).

<b>Nomenclature</b>	
<i>List of notation</i>	
$B$	channel width
$e$	coefficient of restitutition
$E_1$	elastic modulus of grain $i$
$E_2$	elastic modulus of grain $j$
$E^*$	effective elastic modulus
$F_i$	force exerted by grain $i$
$F_{ij}$	force exerted by grain $i$ on grain $j$
$Fr$	Froude number
$g$	acceleration due to gravity
$h$	flow depth
$h_i$	height of grain $i$ above channel base
$h_f$	height of flow after impacting barrier
$K_a$	active earth pressure coefficient
$K_p$	passive earth pressure coefficient
$k_1$	parameter for Beverloo equation describing arch shape
$k_2$	parameter for Beverloo equation describing arch shape
$k_n$	elastic parameter for normal contacts
$k_t$	elastic parameter for tangential contacts
$L$	length of measuring volume
$L_c$	characteristic length scale
$\dot{M}$	mass flux for channel with a slit-structure
$\dot{M}_{\text{open}}$	mass flux for an open channel
$\dot{M}_{\text{norm}}$	normalised mass flux for channel with a slit-structure
$m$	effective grain mass
$m_1$	mass of grain $i$
$m_2$	mass of grain $j$
$n$	number of grain diameters
$N_{\text{fric}}$	Friction number
$N_{\text{gr}}$	number of grains within a region of interest
$N_{\text{sl}}$	number of slits
$P_{\text{drag}}$	pressure due to drag
$P_{\text{slice}}$	pressure on a slice at the barrier
$P_a$	static active pressure
$P_p$	static passive pressure
$P_{\text{total}}$	total pressure
$r$	grain radius
$r^*$	effective grain radius
$r_1$	radius of grain $i$
$r_2$	radius of grain $j$
$s$	slit width
$t$	time (s)
$t_{\text{step}}$	timestep
$TB$	transverse blockage
$U$	bulk flow velocity
$u_i$	velocity of grain $i$
$v\mathbf{n}_{ij}$	normal component of the relative velocity of two interacting grains
$v\mathbf{t}_{ij}$	tangential component of the relative velocity of two interacting grains
$\beta$	angle of the surface of the material relative to the horizontal
$\gamma_n$	normal damping constant
$\gamma_t$	tangential damping constant
$\dot{\gamma}$	shear rate
$\delta$	grain diameter
$\delta\mathbf{n}_{ij}$	overlap distance for grains in normal direction
$\delta\mathbf{t}_{ij}$	overlap distance for grains in tangential direction
$\theta$	channel inclination
$\varepsilon$	angle between the direction of earth pressure & direction perp. to the barrier
$\zeta(e)$	constant depending of the coefficient of restitution
$\mu$	Fluid viscosity
$\nu_s$	solid volume fraction
$\rho_f$	fluid material density
$\rho_s$	solid material density
$\varphi'$	internal friction angle of granular material
$\chi$	constant for pressure

linked with certain mesoscopic flow properties, such as the mean number of contacts [29].

(iii) Even the prospect of developing *empirical* approaches based on field data is challenging because of the poor predictability of natural events [11].

Given the difficulties of dealing with mechanical trapping, it is perhaps unsurprising that quantitative studies and guidelines that discuss design of aspects such as the slit width pertain primarily to inviscid flows (e.g. [11,30–33]). Flows can be quantified as being inviscid or frictional using the friction number  $N_{\text{fric}}$ . Fig. 2 displays estimated friction numbers for studies involving slit-structures – most are inviscid. As such, there is little rational basis for the design of structures intended for mechanically trapping granular material. It is unclear whether existing designs are under- or over-conservative with respect to their intended level of trapping.

There are several studies in the literature that investigate channelised frictional flows interacting with slit-structures (e.g. [16,17,34–39]). Common simplifications include (i) using flows that are entirely dry, thus lying within the frictional regime, and (ii) monodisperse, avoiding complicating factors due to segregation. Quantities of interest include (i) the ability to retard frictional flow material [34–36], (ii) the influence of slit-structure height on energy dissipation [37–39] and (iii) the relationship between the Froude number and trapping, outflow & pileup height [16,17].

Highly-simplified studies of granular material exiting a vertical 2D hopper [40] have shown that outflow differs fundamentally for single-

and dual-slit cases. Given the prevalence of slit-structures with more than one slit (Fig. 1b), it is surprising that a design problem hitherto neglected is how the number and spacing of slits affects trapping and outflow for low values of  $s/\delta$ , where trapping may occur. Table 1 shows a summary of the parameters considered in other studies. Neither (i) the number of slits, nor (ii) the separation therebetween, is quantitatively discussed in relevant guidelines (e.g. [18,41–43]). Gaining a fundamental understanding of this problem is important for improving the scientific basis for slit-structure design. Since it is known that trapping is highly sensitive to  $Fr$  and the ratio  $s/\delta$  for a single slit [16], it can be inferred that the same is true for multiple slits.

In this study, we take a preliminary look at frictional flows impacting multiple-slit-structures using a DEM model based on a physical test first presented in Choi et al. [16]. We adopt dry monodisperse arrays of spheres to model frictional flows, and the mechanisms of mechanical trapping thereof. We vary: (i) the ratio between slit width and grain diameter  $s/\delta$ ; (ii) the number of slits; (iii) the slit separation; and (iv) the Froude number.

## 2. Flume tests

Physical flume tests from Choi et al. [16] were used to calibrate the numerical model in this study. A total mass of 40 kg of uniformly-sized glass spheres were placed in the storage area, and were retained using a spring-loaded gate. The properties of the grains are summarised in Table 2, and come from Choi et al. [16], Cui et al. [44] and Ng et al. [45]. The dimensions of the storage area were  $0.44 \times 0.20 \times 0.50$  m



**Fig. 1.** Slit-structures in the Italian Alps: (a) single-slit-structure; (b) multi-slit-structure.

(Fig. 3a). Two acrylic sheets were held rigid using aluminium angles. These were clamped within the flume 0.9 m downstream from the gate, thus forming a slit-structure (Fig. 3b). The dimensions of the sheets were  $0.01 \times 0.06 \times 0.5$  m. The slit-structure was placed orthogonally to the base of the channel.

After inclining the flume to  $30^\circ$ , the gate was opened remotely [46–48]. A Prosilica GE640 camera faced the flume sidewall to capture the impact kinematics. The framerate was 200 FPS.

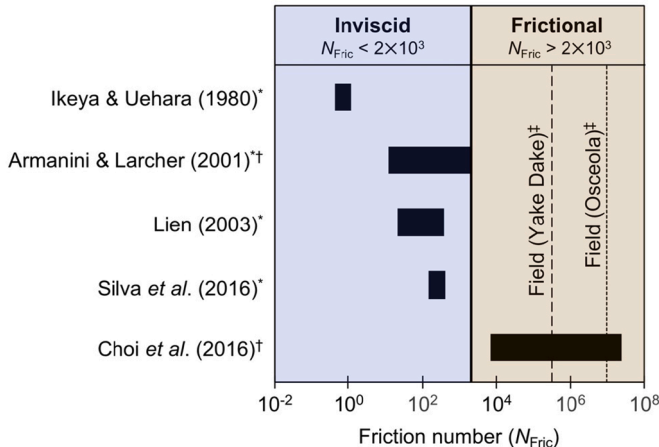
### 3. Numerical modelling

Interaction between frictional flows and slit-structures is heavily dependent on the ratio  $s/\delta$  [16]. As such, the DEM is ideal, since it models individual grains explicitly. Indeed, the DEM has been widely used to understand the dynamics of granular flows impacting obstacles (e.g. [17,19,34,49–58]). In this study, we adopt the open-source DEM

package LIGGGHTS [59]. The version number is 3.7.0, which comes from the Ubuntu 17.10 repository. We use a non-linear contact model, details of which are reproduced in Appendix A. Input parameters are shown in Table 2. The internal friction angle was obtained from a numerical back-analysis presented in Ng et al. [45]. A parametric study was performed in which the internal friction angle was varied. The angle which gave rise to the closest overall flow dynamics to the physical tests was adopted. Since spheres were being modelled, the rolling resistance [60] was set to zero.

#### 3.1. Numerical setup and modelling procedures

The numerical setup for the channelised granular flows experiments matched the geometry of the physical experiment [16]. Like the physical experiment, a total mass of 40 kg of slightly polydisperse discrete elements were generated within the storage container. The



\* Steady-state flows; † Unsteady flows; ‡ Values from Iverson & Denlinger (2001) from debris flows in the field.

**Fig. 2.** Range of friction numbers covered by flows in various studies relating to slit-structures. Only studies which provide sufficient information on flow properties to estimate  $N_{\text{flic}}$  are included.

polydispersity reduces crystallisation effects [17,61]. After the grains had settled, the direction of gravity was changed, simulating inclination of the flume. After the grains had stopped moving, one wall of the storage area was deleted, facilitating dam-break [46,48]. The flows then interacted with a slit-structure with either one slit ( $N_{\text{sl}} = 1$ ; Fig. 3b) or two slits ( $N_{\text{sl}} = 2$ ; Fig. 3c). Grains that moved at least 3 m downstream from the slit-structure were deleted to reduce computational time. By this point, the grains were highly dispersed, so there was no effect on the interaction between flow and slit.

### 3.2. Scaling & flow characterisation

Three well-defined parameters in the literature are said to govern the rheological behaviour of granular flows: the ratio between flow depth and grain size ( $h/\delta$ ), the solid volume fraction  $\nu_s$ , and the Froude number [13–15,38,62]. The solid volume fraction and ratio  $h/\delta$  are both linked to the Inertia number [63], a constitutive law for granular flows that can be used to differentiate between frictional (dense) and collisional (dispersed) flow regimes. Lower solid volume fractions tend to imply more collisional flows, as do small numbers of grains per unit depth.

The Froude number [11–15] is given by:

$$Fr = \frac{U}{\sqrt{gh\cos\theta}} \quad (2)$$

where  $U$  is the mean flow velocity,  $g$  is the acceleration due to the Earth's gravity,  $h$  is the depth of the flow and  $\theta$  is the inclination of the channel. For unsteady granular flows, the quantities  $h/\delta$ ,  $\nu_s$  and  $Fr$  are in constant flux [45].

Fig. 4 shows characteristic curves for  $\nu_s$ ,  $h/\delta$  and  $Fr$  for two channel inclinations: 22° and 30°. These curves were obtained from open-channel simulations in this study. The DEM model was used to calculate quantities along the length of the flow as it passed a static measuring volume placed 0.9 m downstream from the gate [45]:

$$h = \frac{2}{N_{\text{gr}}} \sum_{i=1}^{N_{\text{gr}}} h_i \quad (3)$$

$$\nu_s = N_{\text{gr}} \frac{(4/3)\pi r^3}{hBL} \quad (4)$$

$$Fr = \frac{1}{N_{\text{gr}}} \sum_{i=1}^{N_{\text{gr}}} \frac{u_i}{\sqrt{gh_i \cos\theta}} \quad (5)$$

where  $N_{\text{gr}}$  is the number of grains in the measuring volume;  $h_i$  is the

height of the centroid of grain  $i$ ;  $r$  is the grain radius;  $B$  is the channel width;  $L$  is the length of the measuring volume; and  $u_i$  is the velocity of grain  $i$ . Eq. (3) is calculated as twice the mean flow depth, rather than simply finding the highest grain, to avoid skewing the data due to saltating grains. Eq. (4) is the ratio of total grain volume to the volume occupied by the flow. In Eq. (5), an equivalent Froude number is computed for each grain, after which a mean is taken [45].

Fig. 4a shows the ratio  $h/\delta$  against the normalised flow position. The flow depth is smallest at the front and the tail of the flows. The maximum flow depth recorded for both channel inclinations is similar to that physically measured in Choi et al. [16] for two equivalent open-channel flows. Fig. 4b shows the volume fraction (ordinate) as it changes along the length of the flow  $L$  (abscissa). For both flows (22° and 30°) the front is highly dispersed; the density is at a maximum near the body of the flow. The dispersed front is related to the small frontal flow depths: at the front, confining stress is minimal, so grains are able to move around freely (see also [45]).

Fig. 4c shows how  $Fr$  varies along the length of the flow;  $Fr$  is around 9.5 at the front for the 22° case, and 11 for the 30° case.  $Fr$  decreases near the middle of the flow as the flow thickens (Fig. 4b) and the flow velocity is slightly reduced. This is consistent with results from Ng et al. [45]. A comparison of  $Fr_{\min}$ , estimated from physical tests in [16], shows that the computed  $Fr$  is higher for both channel inclinations. Given the close match with the flow depth shown in Fig. 4a, this is probably because of differences in the flow velocity, congruent with the aforementioned rate-dependent mobilised friction angle. For convenience, we refer to the channel inclination throughout the rest of the manuscript: even though  $h/\delta$ ,  $\nu_s$  and  $Fr$  govern flow dynamics, they are all transient.

### 3.3. Numerical simulation plan

Two numerical test series were performed to investigate the effects of: (i) the ratio between the slit opening and the grain diameter  $s/\delta$ ; and (ii) the slit separation. The ratio  $s/\delta$  is related to the transverse blockage, which is the proportion of the channel blocked by the slit-structure:

$$TB = \frac{B - \sum s}{B} \quad (6)$$

where  $B$  is the channel width and  $s$  is the slit width. The physical meaning of the transverse blockage is the proportion of the channel blocked by the slit-structure.

Across both series, the number of slits was varied as one and two.

**Table 1**  
Summary of geometric parameters adopted in studies on frictional flows impacting slit-structures.

Study	Study type	Material	Channel width (m)	Obstacle width (m)	Number of slits $N_{sl}$	Slit width $s$ (m)	Grain diameter $\delta$ (m)	Ratio of $s/\delta$
Hákonardóttir et al. [35,36]	Physical flume	Snow	2.5	0.6	3	0.4	< 0.1	> 4
Teufelbauer et al. [49]	DEM (PFC3D)	(Quartz Sand)	1.1	0.16	2	$\infty$	0.005	-
Teufelbauer et al. [34]	DEM (PFC3D)	(Quartz Sand)	1.1	0.01	11	0.09	0.005	18
Choi et al. [37]	Physical flume	LB sand	0.2	0.02	3	0.04	0.0006	67
Choi et al. [38,39]; Law et al. [54]	DEM (LIGGGHTS)	LB sand	0.2	0.02	3	0.04	0.004	10
Choi et al. [16]	Physical flume	Glass spheres	0.2	0.04-0.09	1	0.02-0.12	0.01-0.04	$2 < s/\delta < 8$
Leonardi et al. [58]	DEM	(Glass spheres)	0.2	0.08-0.20	1	0.00-0.12	0.01-0.04	$2 < s/\delta < 12$

The ratio  $s/\delta$  was varied from 2 to 20, corresponding to transverse blockages ranging from 0.0 to 0.9. The slit separation only applied to cases with two slits. The slit separation was varied from  $0\delta$ , which is effectively a single slit, to  $12\delta$ . The upper bound was constrained by the width of the flume and slit size. The channel inclination was varied as  $22$  and  $30^\circ$  to simulate different  $Fr$ . The numerical simulation plan is shown in Table 3.

### 3.4. Numerical model calibration

Fig. 5 shows a comparison between physical and computed flow kinematics impacting a slit-structure. For both cases, the channel inclination is  $30^\circ$ , the slit opening is 50 mm, and the grain size is 10 mm. At  $t = 0.0$  s (Fig. 5i), a wedge-shaped flow front with a frontal velocity of 3 m/s approaches the slit-structure for both physical and numerical cases. At  $t = 0.2$  s (Fig. 5ii), the flow has impacted the slit-structure; run-up [39,64] and outflow [16] occur simultaneously. For  $t = 0.4$  through to  $t = 0.8$  s (Fig. 5iii to v), the flow piles up in front of the slit-structure [16] on top of a largely stagnant ‘dead-zone’ [65,66]. Additionally, the rate of outflow diminishes over time, as reflected by the angle subtended between the upper layer of outflowing material and the base of the flume. It is worth noting that the shape of the pileup is slightly different between the physical and numerical cases; this is most apparent in Fig. 5v, where the pileup is steeper in the physical experiment. The pileup is also slightly thicker upstream for the numerical case. This is evident in Fig. 5v. Both phenomena are likely indicative of the importance of the dependence of granular friction angles on the friction angle [63], which cannot be captured using the contact model adopted in this study. Nevertheless, Fig. 5 shows overall that the numerical model is able to capture the essential characteristics of interaction between the flow and the structure, lending confidence to its use throughout the rest of this study.

## 4. Interpretation of results

### 4.1. Effects of number of slits on discharge

Fig. 6 shows top-down views of flows impacting slit-structures with varying distances between the slits. For each case, the channel inclination was  $30^\circ$ , the transverse blockage was 0.75 and  $s/\delta$  was 2.5. Colour contours of the spatial distribution in the flow velocity are shown (as in [40]), with red grains moving at 0.5 m/s or more and dark blue grains being static. For each case, three instants are shown. For  $n\delta = 1$  (Fig. 6a), the zone of influence of the two slits overlaps; the mass of moving grains extends more than ten particle diameters upstream. For  $n\delta = 8$  (Fig. 6b), the region between the two slits is mostly static, as is the case for  $n\delta = 12$  (Fig. 6c). Furthermore, the mass of moving grains near the slits for the latter two cases does not extend as far upstream as for  $n\delta = 1$ , since the shear zones do not overlap.

Fig. 7 shows discharge histories for three cases: (i) an open-channel, with no slit-structure; (ii) a slit-structure with a single slit; and (iii) a slit-structure with two slits. For the latter two cases, the transverse blockage was the same ( $TB = 0.5$ ), where  $TB$  is calculated using Eq. (6).  $TB = 0.5$  was chosen to avoid grains becoming trapped as shown from data from Choi et al. [16]. The ordinate shows the mass outflow rate. The mass outflow rate is normalised by the peak outflow rate recorded for the open-channel case. The abscissa shows the time.

The outflow rate for the open-channel case increases sharply with time, reaching the peak (unity) at around 0.4 s. The rate then decreases, reaching zero at 1.5 s. The change in outflow rate with time is consistent with the scaling curves presented in Fig. 4: the front and tail of the flow are relatively disperse, with a volume fraction of around 0.36, as opposed to at the centre where it is almost 0.50. As such, the mass outflow rate is lower than at the longitudinal centre, i.e. at the body of

**Table 2**

Parameters adopted in numerical simulations.

	Physical tests	Numerical simulations	Reference
Diameter (m)	$0.010 \pm 0.001$		–
Material density ( $\text{kg}/\text{m}^3$ )	2650		–
Internal friction angle ( $^\circ$ )	19.8		Ng et al. [45]
Interface friction angle ( $^\circ$ )	16.6		Choi et al. [16]
Young's modulus (Pa)		$10^8$	Ng et al. [45]
Poisson's ratio		0.3	
Rolling resistance		0	
Contact model		Hertz	

the flow [67]. It should be noted that the properties of the tail of the flow have little influence on the interaction between the flow and the structure [45].

The peak outflow for the two cases with a slit-structure occurs at almost the same time as the open-channel case, although the magnitude of the outflow is greatly reduced. The peak outflow rate for  $N_{\text{sl}} = 1$  is  $\sim 60\%$  that of the open-channel case, whilst it is  $\sim 40\%$  for  $N_{\text{sl}} = 2$ . Consistent with these reduced peak outflow rates, adopting two slits rather than one causes the total outflow time to increase from 6 s to 9 s.

#### 4.2. Contact durability

To quantify the degree of interaction between slits, we have developed a simple algorithm for investigating at the durability of contacts between pairs of grains within a region of interest.

LIGGGHTS [59] is used to output contacts between grains at each timestep, taken at intervals of 1 ms. Pairs of IDs for contacting grains, as well as the spatial positions thereof, are recorded. A list is made of the contact IDs at each timestep for grains which fall within the region of

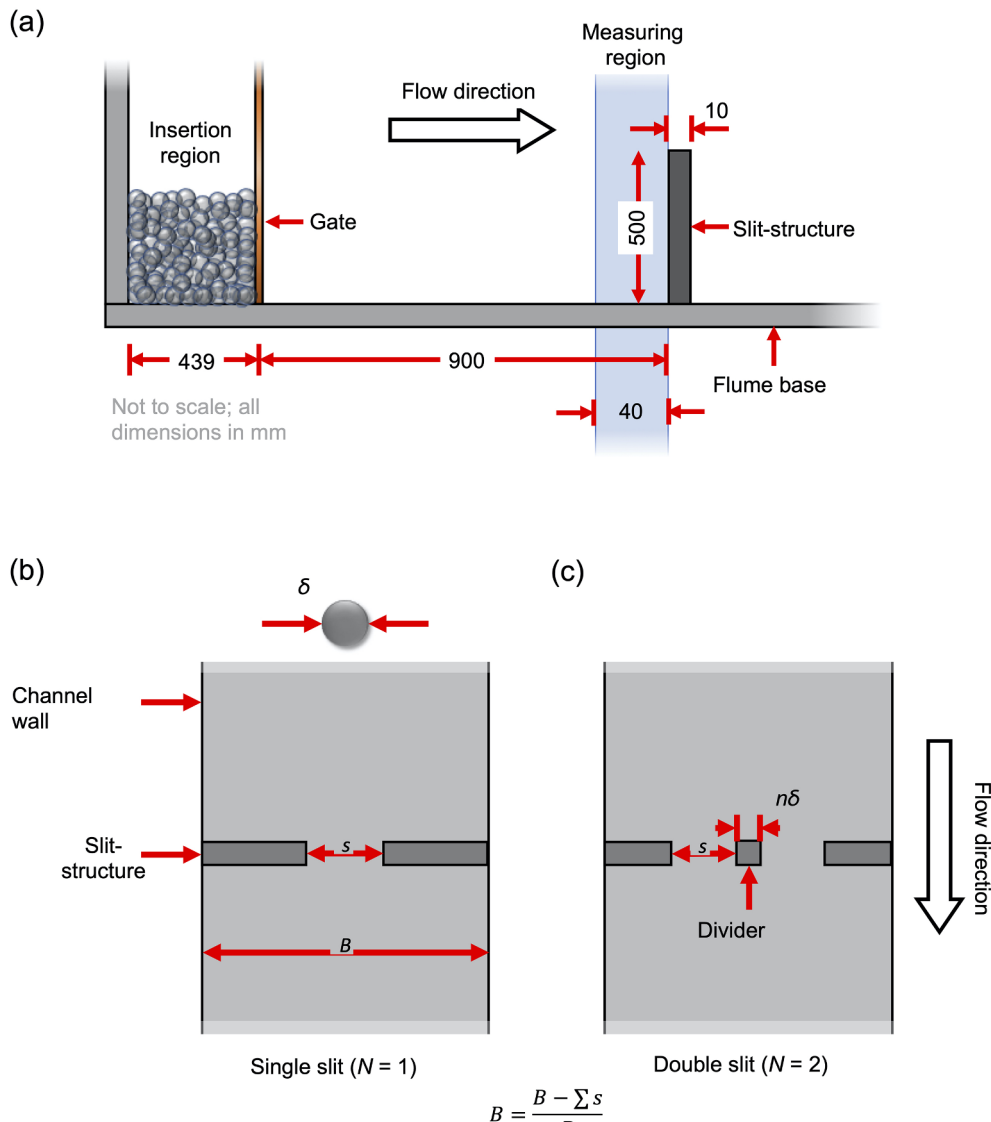


**Fig. 3.** (a) Side-view schematic of the physical flume model (geometrically identical to the DEM model); (b) top-down schematic of a single-slit-structure; (c) top-down schematic of a dual-slit-structure.

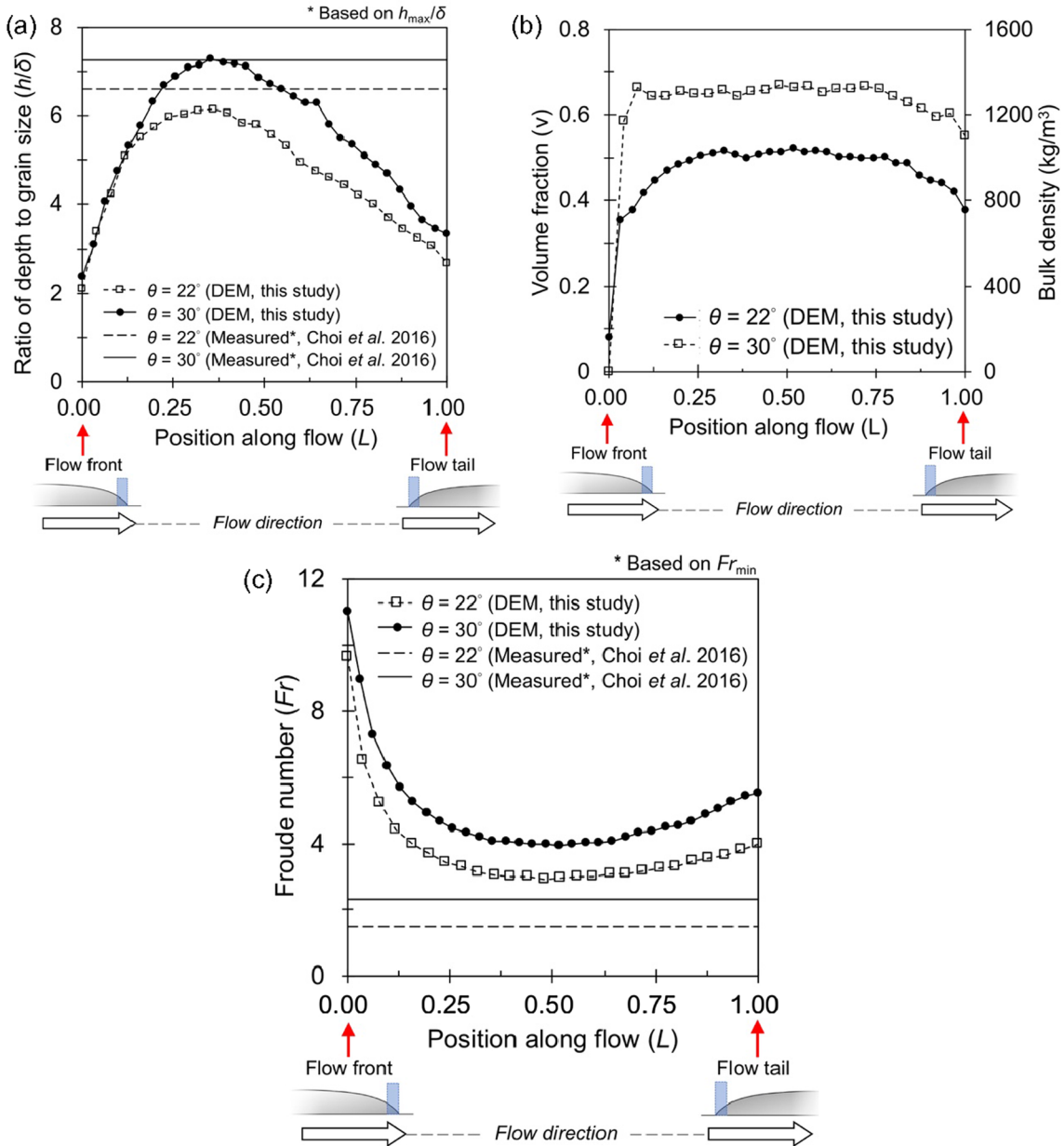


**Fig. 4.** Characteristic curves for open-channel flows: (a) ratio of depth to grain size; (b) volume fraction; (c) Froude number. The reference lines on parts (a) and (c) represent maximum flow depths and minimum Froude numbers respectively, estimated from physical tests in Choi et al. [16].

interest. The IDs for adjacent timesteps are then compared. If a pair of IDs persists, occurring in both timesteps, it is denoted as ‘durable’ (see also [68]). The total number of ‘durable’ contacts for each timestep is then divided by the total number of contacts, producing a value between zero and unity. Zero indicates that no contacts are maintained between timesteps, tending towards a collisional regime (see [63]). In contrast, unity indicates that all contacts are maintained, tending towards a frictional regime [63]. Although the exact output value is a function of the timestep adopted, as long as the timestep is the same for each case considered, cases can be fairly compared. A flow chart of this procedure is shown in Fig. 8.

Fig. 9a and b show the contact durability calculated using the above procedure. The region of interest selected is the space directly in front of the divider, and thus varies between cases. Contact durability is on the ordinate, whilst time (in seconds) is on the abscissa. In Fig. 9a, the four lines represent average values for contact durability for single-slit-structures (see Fig. 3b). The transverse blockage  $TB$  ranges from 0.0

(open channel) to 0.8 (an opening of  $s/\delta$  of 4). Time  $t = 0$  s approximately corresponds to when the flow starts to impact the slit-structure. As expected, there is a clear increase in the durability of contacts as the transverse blockage is increased. This shows that the link between trapping efficiency and increased transverse blockage observed in Choi et al. [16] is due to the ability of the slit-structure to prolong inter-grain contacts.

In Fig. 9b, both lines correspond to a dual-slit-structure (see Fig. 3c). The spacing between the slits is 2 $\delta$  and 12 $\delta$ . For both cases, the contact durability initiates around 0.7, as the flow starts to impact the structure, and then increases. At time  $t = 1$  s, both cases have reached their final values. For 2 $\delta$ , the average contact durability is 0.86, whilst for 12 $\delta$  the durability is around 0.94. This indicates that wider dividers produce more frictional flows, at least in the region directly in front of them. This matches with the velocity contours of the flow in Fig. 6a, b and c, where grains in the region behind the divider move progressively slower as the slits are moved further apart.

**Table 3**  
Test plan.

Test series	Number of slits ( $N_{sl}$ )	Slit separation ( $N\delta$ )	Ratio between slit size and grain diam. ( $s/\delta$ )	Transverse blockage ( $B-\Sigma s)/B$	Channel incl. ( $^\circ$ )
Open channel	1	—	20	0.00	22, 30
Transverse blockage	1, 2	1	2 3 4 5 6 8 10 12 14 16	0.90 0.85 0.80 0.75 0.70 0.60 0.50 0.40 0.30 0.20	22, 30
Slit separation	1, 2	0, 1, 2, 3, 4, 5, 6, 7, 8	4 5 6 8	0.80 0.75 0.70 0.60	22, 30

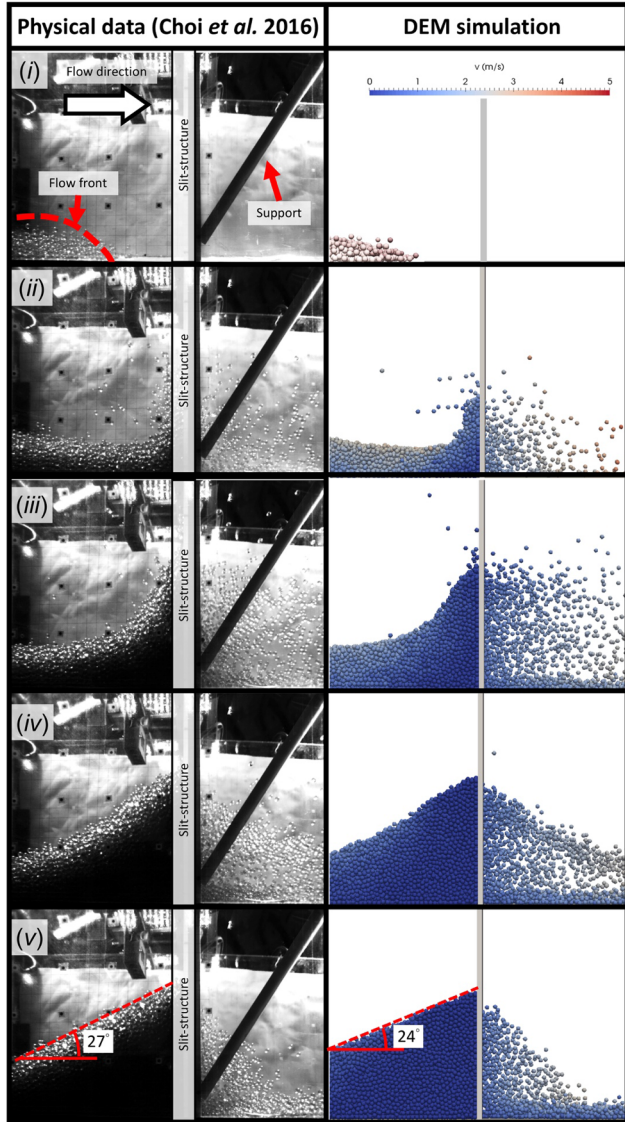


**Fig. 5.** Comparison of physical and numerical flow dynamics. (i)  $t = 0.0$  s; (ii)  $t = 0.2$  s; (iii)  $t = 0.4$  s; (iv)  $t = 0.6$  s; (v)  $t = 0.8$  s.

#### 4.3. Pressure distribution

To gain further insight into the interaction between slits, the contact force on the barrier during outflow was investigated. Contact pressure was extracted from the divider (Fig. 3c) from a series of rectangular measurement sections. Each measurement section was  $4\delta$  in length, parallel to the direction of flow. The region matched the width of the divider. The following equation was then used to compute the total pressure:

$$P_{\text{slice}} = \frac{1}{2n\delta^2} \sum_{i=1}^N F_i \quad (7)$$

where  $n\delta$  is the width of the divider in terms of grain diameters. The pressure on the barrier was then compared with the theoretical static active earth pressure and theoretical static passive earth pressure, both assumed to have a triangular distribution with depth:

$$P_a = K_a \gamma_s \rho_s g H \quad (8a)$$

$$P_p = K_p \gamma_p \rho_s g H \quad (8b)$$

where  $K_a$  is the active static earth pressure coefficient;  $K_p$  is the passive static earth pressure coefficient; and  $H$  is the depth below the top of the flow. The active earth pressure was calculated using the following relationships [69]:

$$K_a = \frac{\cos^2(\phi' - \theta)}{\cos^2(\alpha)\cos(\varepsilon + \alpha) \left[ 1 + \sqrt{\frac{\sin(\phi' + \varepsilon)\sin(\phi' - \beta)}{\cos(\varepsilon + \theta)\cos(\beta - \theta)}} \right]^2} \quad (9a)$$

$$K_p = \frac{\cos^2(\phi' - \theta)}{\cos^2(\alpha)\cos(\varepsilon + \alpha) \left[ 1 - \sqrt{\frac{\sin(\phi' + \varepsilon)\sin(\phi' - \beta)}{\cos(\varepsilon + \theta)\cos(\beta - \theta)}} \right]^2} \quad (9b)$$

where  $\phi'$  is the internal friction angle of the granular material;  $\theta$  is the angle of inclination of the barrier relative to the vertical, and is  $25^\circ$  for all tests;  $\varepsilon$  is the angle between the direction of the earth pressure and the direction perpendicular to the barrier, and is assumed to be  $0^\circ$  for all tests; and  $\beta$  is the angle of the surface of the material relative to the horizontal. These quantities are shown graphically in Appendix B, Fig. B1.

Fig. 10 shows how the mean pressure along the divider varies with height for two cases:  $n\delta = 1$  (Fig. 10a) and  $n\delta = 6$  (Fig. 10b). Two timesteps are shown for each case, both of which correspond to after the initial impact. Pressure due to drag is of the same form as dynamic pressure, i.e.  $\chi\rho U^2$ , where  $\chi$  is an impact coefficient [70–72]. Assuming the pressure on the wall to be the sum of dynamic and static pressure, and assuming the static pressure to be closer to the active pressure [48,73], the drag force can be computed as  $P_{\text{drag}} = P_{\text{total}} - P_a$ . Fig. 10a shows that the total pressure for both timesteps shown is more than double the theoretical static active load near the top of the pileup, implying a correspondingly high drag component. The peak pressure at  $t = 0.8$  s is around 2.3 kPa. By contrast, in Fig. 10b it can be seen that the drag force is much lower across the height of the wider divider. The total peak pressure for  $t = 0.8$  s is less than 5% higher than the theoretical static pressure [69]. Here, the pressure extracted from the DEM model is 1.5 kPa. Furthermore, this extracted pressure is 35% lower than that for  $n\delta = 1$ . The maximum drag force occurs at around 1/3 of the depth of the pileup, implying that outflow is highest near there. This suggests that: (i) the drag force is not negligible, in contrast to existing recommendations where it is not considered (e.g. [18,41–43]); and (ii) the more separation between slits, the smaller the mean drag forces on the slit-structure.

Furthermore, both parts of Fig. 10 show that the mean pressure along the height of the divider is strongly related to its width. This fits with the results for contact durability in Fig. 9, wherein contact durability increases as the width of the divider increases. It can thus be

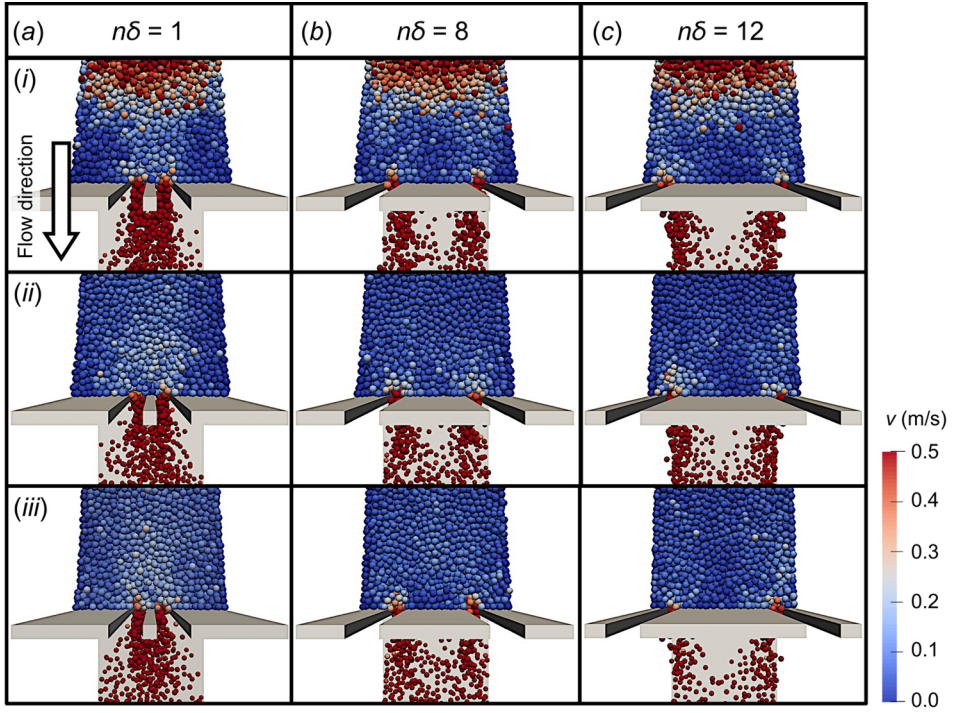
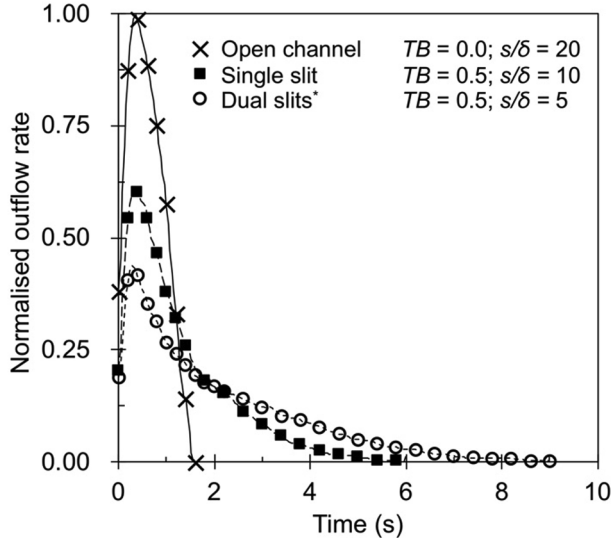


Fig. 6. Velocity profiles for  $TB = 0.75$  at  $30^\circ$ . Times are separated by  $0.8\text{ s}$  (20 timesteps, at  $0.04\text{ s}$  per timestep): (i)  $t = 0.6$ ; (ii)  $t = 1.4$ ; (iii)  $t = 2.2\text{ s}$ .



\* Width of divider = 1 $\delta$

Fig. 7. Comparison of normalized outflow rates for three cases: an open channel (control case), a single-slit-structure and a dual-slit-structure.

inferred that the reduction in mean drag for a wider divider subjects grains between the slits to a lower degree of shearing. As an aside: results from Figs. 9 and 10 also have implications for net barriers designed to impede granular flows (e.g. [74]). The drag forces are likely to be a key design consideration, especially if the thickness of individual wires is small compared to the grain size.

#### 4.4. Trapping efficiency

Fig. 11 includes four graphs, all of which show the trapping efficiency  $E$  on the ordinate. The term ‘trapping efficiency’ [33,75–78] is used here to describe the proportion of flow material retained upstream of a slit-structure [16]. Zero indicates that all the flow material travels

downstream, whilst unity means that all the material becomes trapped. Fig. 11a and b correspond to channel inclinations of  $22$  and  $30^\circ$  respectively, and show the transverse blockage (Eq. (6)) on the abscissa. Fig. 11c and d also correspond to channel inclinations of  $22$  and  $30^\circ$ , but instead show the ratio  $s/\delta$  on the abscissa.

Five lines are shown in Fig. 11a, corresponding to slit separations of  $0 < n\delta < 6$ . The line for  $n\delta = 0$  corresponds to a single slit. The two shaded regions demarcate zones (i) where trapping does not occur, i.e. ‘self-cleaning’ and (ii) where more than 90% of the material is trapped. Explicitly demarcating regions in this way is an important first step for slit-structure design to ensure structures behave as expected. It should be noted that no such guidelines exist in existing recommendations, i.e. VanDine [41], MLR [42], SWCB [43], and NILIM [18].

As the slits are moved further apart, the trapping efficiency increases. The largest change occurs for  $TB = 0.85$ . The trapping efficiency for the single slit is almost zero. In contrast, for all the double slit cases, the trapping efficiency is greater than 90%. For  $TB = 0.80$ , the trapping efficiency is also very sensitive to the slit spacing. At  $TB = 0.80$ , the trapping efficiency is zero for  $n\delta = 0$  and around 0.8 for  $n\delta = 1$ . The increase in trapping efficiency is linked with the reduced interaction between outflowing material. More specifically: even if stable arches form throughout the depth of the granular mass at one slit, shearing from grains exiting the other slit can break otherwise stable arches, as reflected by the increase in contact durability shown in Fig. 9. As such, the probability of stable arches forming throughout the depth of the flow mass at both slits simultaneously increases with the width of the shearing zone. The width of the shearing zone increases as the slits are moved apart, but is not directly related to the transverse blockage.

A similar picture emerges from Fig. 11b (for a channel inclination of  $30^\circ$ , and thus a higher Froude number along the length of the flow; Fig. 4c). Interestingly, the relationship between trapping efficiency and transverse blockage changes does not change qualitatively. The lines shift to the right, corresponding to a decrease in the size of the trapping zone, and an increase in the size of the self-cleaning zone (corresponding to a change in transverse blockage of 0.05). This is consistent with the effects of increasing  $Fr$  observed in Choi et al. [16]. This reliance on  $Fr$  implies that it is insufficient to capture the trapping

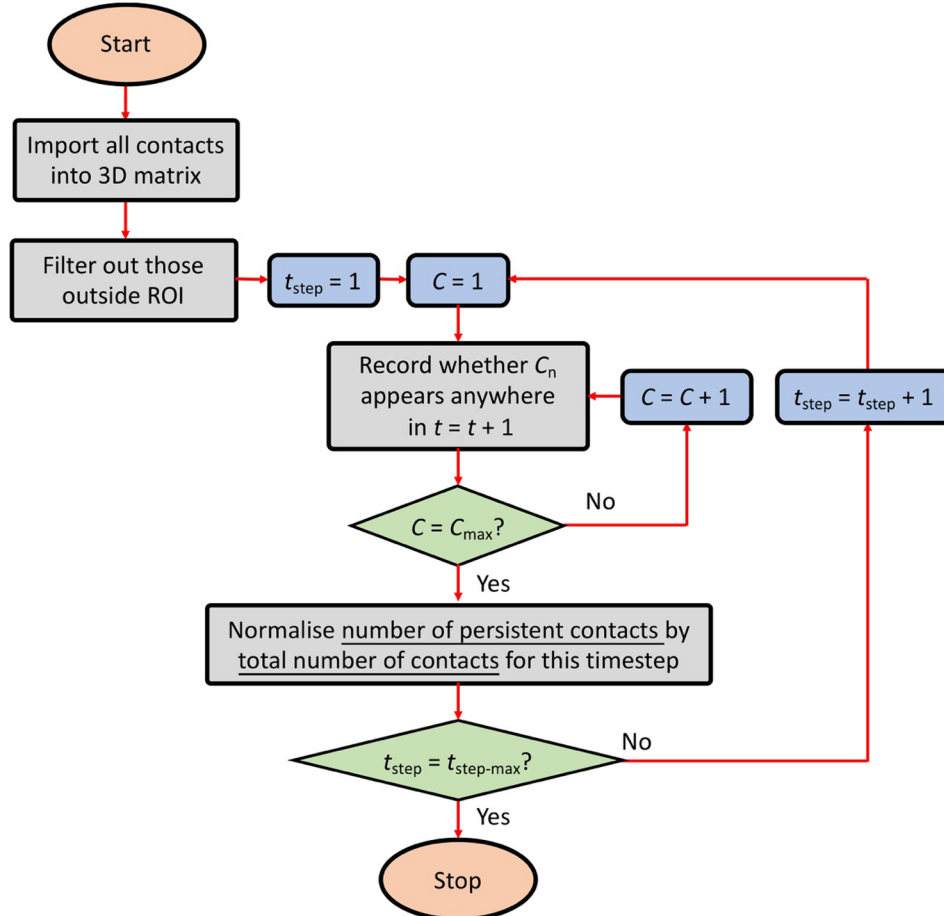


Fig. 8. Algorithm for contact duration.

efficiency without considering the flow dynamics. It should be noted that existing guidelines, such as MLR [42], SWCB [43] and NILIM [18] do not consider the flow dynamics.

Fig. 11c shows the same data as Fig. 11a, but with the ratio  $s/\delta$  plotted on the abscissa instead. As such, the line corresponding to  $n\delta = 0$  has a transverse blockage half that of the other cases. In addition to the shaded zones, the recommendations for  $s/\delta$  given by MLR [42] and SWCB [43] are shown. For a given value of  $s/\delta$ , the trapping efficiency for the single slit is higher than for two slits. The trapping efficiency decreases further as the slits move closer together. This is consistent with the aforementioned effects of shear interaction between slits (Figs. 9 and 10) (see also results from 2D cases in [40]). Furthermore, for the Froude curve adopted, the guidelines from MLR [42] and SWCB [43] would cause the trapping efficiency to fall in the unstable region shaded in white. Given the uncertainties in the actual Froude curve in the field, as well as the grain size, this could cause a structure to become blocked or undergo massive discharge unexpectedly. Fig. 11d shows that the relationship between trapping efficiency and  $s/\delta$  holds for higher  $Fr$ .

Fig. 11a to d collectively demonstrate that  $TB$  and  $s/\delta$  are linked, but not equivalent. Specifying the design for a slit-structure exclusively in terms of one or the other (as in [18,42–43]), and disregarding the number of slits or the spacing thereof, may cause the trapping/cleaning behavior to deviate from that expected. This is especially pertinent since the three recommendations listed above all cover slit-structures with multiple slits. Furthermore, engineers should be aware of the extreme sensitivity of the trapping efficiency when designing slit-structures. Regardless of whether the structure is intended for trapping or self-cleaning, the unstable zone should be avoided to minimize the chance of surprises.

#### 4.5. Influence of slit number and transverse blockage on the peak outflow rate

As has already been shown in Fig. 7, interaction between dry granular flows and slit-structures is unsteady. As such, a key design consideration for engineers is related to the peak outflow rate [79]. The Beverloo law [80,81] has been widely used for granular flows exiting slits in hoppers, and can be adapted as a reference for flows in this study, although different characteristic length- and time-scales are required. The Beverloo law is given by:

$$\dot{M} = k_1 \nu_s \rho_s g^{1/2} (s - k_2 \delta)^{5/2} \quad (10)$$

where  $\dot{M}$  is the mass flux;  $k_1$  and  $k_2$  are parameters describing the shape of the arch, the latter depending on grain properties such as the friction angle;  $\nu_s$  is the solid volume fraction;  $\rho_s$  is the solid material density;  $g$  is the acceleration due to the Earth's gravity;  $s$  is the slit width; and  $\delta$  is the grain density. By writing it in terms of a characteristic length-scale,  $L = (s - k_2 \delta)$ , it is easier to understand its physical meaning:

$$\dot{M} = k_1 \nu_s \rho_s L \cdot L (gL)^{1/2} \quad (11)$$

In other words, the Beverloo law gives the mass flow rate for material with an initially near-zero velocity exiting a rectangularly-shaped slit. A simple dimensional analysis reveals that the term  $L = (s - k_2 \delta)$  is relevant only for the width of the slit considered in this study. The term  $(gL)^{1/2}$  does not properly characterise the outflow velocity, which is not dominated by gravitational forces (Fig. 4c) – at least for the peak outflow shown in Fig. 7. As such, the flow depth  $h$  and pre-impact velocity  $U$  are adopted as the vertical length-scale and time-scale respectively. Furthermore, a term  $N_{sl}$  is inserted to account explicitly for the number of slits:

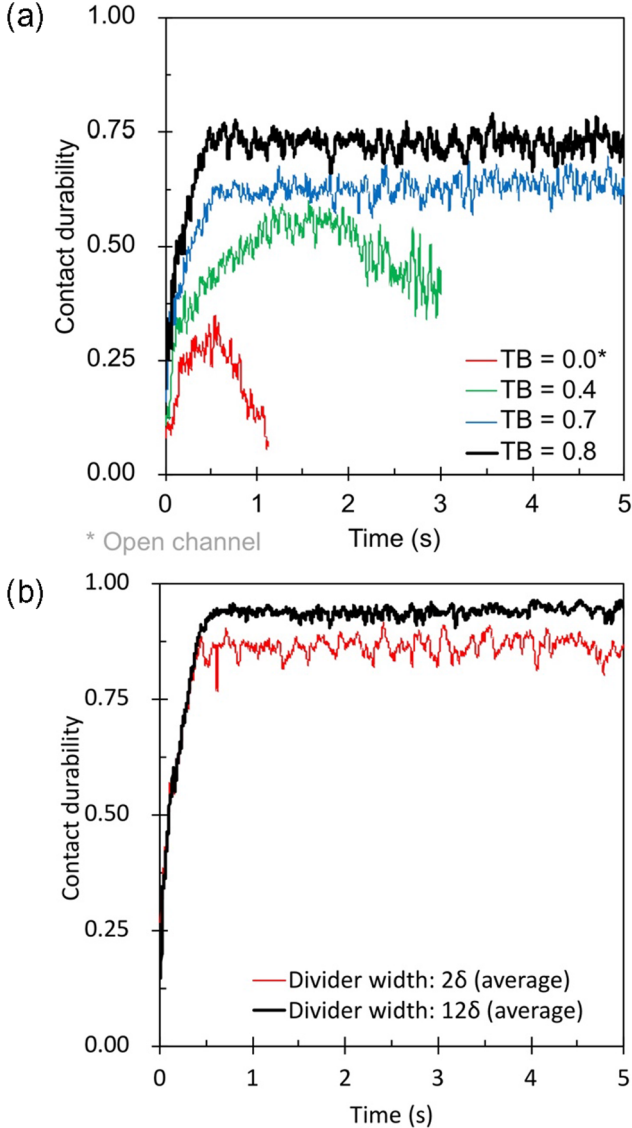


**Fig. 9.** Contact duration for flows interacting with slit-structures. The channel inclination is 30° for all cases. (a): Single-slit-structure with varying transverse blockage, where the region of interest is in front of the slit; (b) dual-slit-structure with varying slit-spacing, where the region of interest is in front of the divider and  $TB = 0.75$ .

$$\begin{aligned} \dot{M} &= k_1 N_{sl} \nu_s \rho_s (s - k_2 \delta) h U \quad \text{for } s \geq \delta \\ \dot{M} &= 0 \quad \text{for } s < \delta \end{aligned} \quad (12)$$

We then normalise the mass outflow rate by that of the peak outflow for an open channel, so as to better assess the effectiveness of the slit-structure:

$$\dot{M}_{norm} = \frac{\dot{M}}{\dot{M}_{open}} = \frac{N_{sl}(s - k_2 \delta)}{(B - k_2 \delta)} \quad \text{for } s \geq \delta \quad (13)$$

where  $B$  is the channel width. This form of the equation implies that neither the depth  $h$  nor the velocity  $U$  affect the normalised mass outflow rate. It should be noted that this assumption is probably not entirely valid, since the slit-structure tends to both reduce the velocity and increase the flow depth upstream [16].

Fig. 12a and b show the normalised peak outflow rate against the transverse blockage for  $N_{sl} = 1$  and  $N_{sl} = 2$ , for the channel inclinations of 22° and 30° respectively. The ‘self-cleaning’ and ‘trapping’ regions deduced from Fig. 11 are overlaid for reference. ‘Self-cleaning’ is defined as material tending not to accumulate permanently behind a

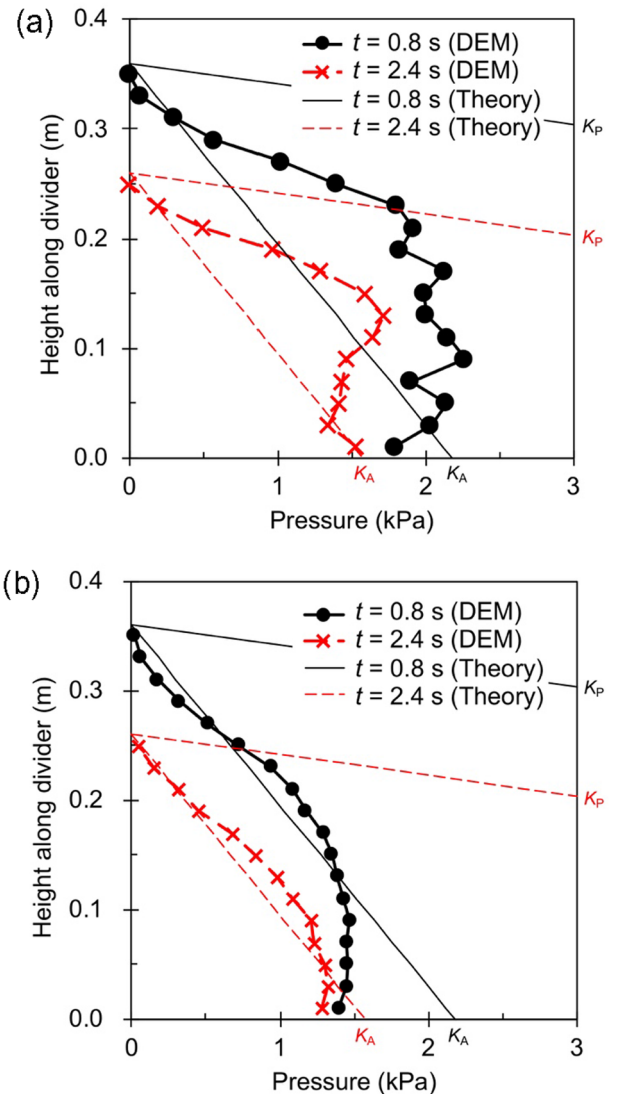


**Fig. 10.** Force profile on divider. (a)  $n\delta = 1$ ; (b)  $n\delta = 6$ . The channel inclination is 30° for both cases; the sampling time was chosen to show the forces on the divider during outflow. The theoretical lines for earth-pressure are for granular material on a sloped surface in contact with an inclined wall and come from CGS [69].

structure. Furthermore, reference lines based on Eq. (13) are included.

Fig. 12a shows that for 22° and both  $N_{sl} = 1$  and  $N_{sl} = 2$ , the normalised peak outflow rate increases non-linearly as the transverse blockage is reduced, in contrast to Eq. (13) which suggests a linear relationship. This is related to the relationship between pileup height and velocity. For higher transverse blockage, where the slits are narrower, the pileup increases [16]. Overall, however, Eq. (13) is able to provide a good approximation of the peak outflow rate for both single- and dual-slit cases.

Fig. 12b shows the normalised peak outflow rate for 30°. Since it was assumed in Eq. (13) that the velocity and flow depth cancel, the reference lines are identical to those in Fig. 12a. The same general trend of the outflow rate increasing as the transverse blockage decreases is shown; the degree of non-linearity is qualitatively similar to that shown in Fig. 11a. However, the outflow rate for 30° is proportionately higher compared to the theoretical lines than for 22°. This suggests that the channel inclination affects the length- and time-scales relating to the characteristic velocity and flow-depth. This is certainly true for the pileup height, which increases with the Froude number [16,82], and hence the channel inclination (Fig. 4c), so assuming that  $h$  does not

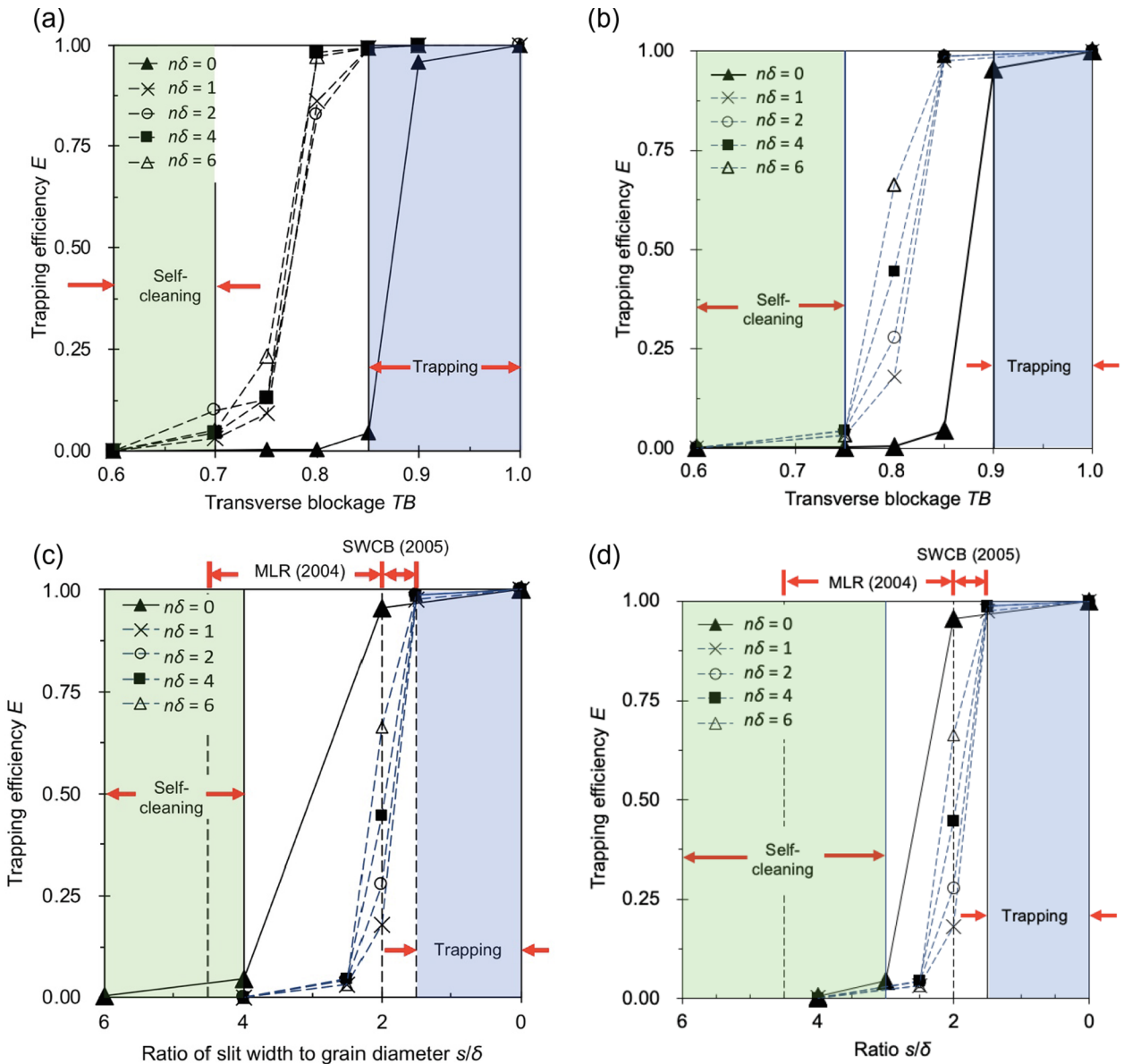


**Fig. 11.** Trapping efficiencies: (a) as a function of transverse blockage for a channel inclination of 22°; (b) as a function of transverse blockage for a channel inclination of 30°; (c) as a function of  $s/\delta$  for a channel inclination of 22°; (d) as a function of  $s/\delta$  for a channel inclination of 30°.

change may be under-conservative.

In summary, Fig. 12 shows that there is a near-linear relationship between the peak outflow rate and the transverse blockage, relative to open-channel flow. The modified Beverloo law for channelised flows (Eq. (13)) is able to capture the basic relationship between outflow and transverse blockage for one or two slits. This suggests that estimating the outflow rate can be simply estimated after designing a slit-structure for either self-cleaning or trapping. However, a safety factor should be applied to results calculated from Eq. (13) to account for the potential underestimate of the outflow rate. A larger-than-expected peak outflow rate would tend to increase the downstream Froude number. This would necessitate changes to other mitigative structures in the system, such as making them taller [16] and having narrower slits, as implied by Figs. 11 and 12.

## 5. Discussion of limitations

Design guidelines for slit-structures are empirical [18,41–43]. Improving the state-of-the-art requires systematic, repeatable tests. To

create well-characterised flows, nearly-monodisperse spheres were adopted in this study, which are immune to effects caused by segregation (see [83]). Such flows have limited bulk compressibility [84], affecting the packing fraction and hence the behaviour of the flow as it passes through a slit [85].

In addition, the scale of the model is considerably smaller than prototype flows. Therefore, we would expect that larger flow and deposition depths would be observed at larger scales. Larger flow and deposition depths are anticipated to cause higher effective stresses, thereby altering the stability of force chain networks. The stress state should also affect the volumetric change of the flow material [63], with corresponding differences in dilatory/contractive behaviour. Furthermore, it is expected that at higher stress and energy levels that grain crushing may occur as well [86]; this would (i) change the characteristic grain size, and hence the ratio  $s/\delta$  and (ii) dissipate energy through cracking. Given these limitations, it is not currently possible to assess whether the results from this study are conservative. Further testing at other scales and under other conditions will be required to establish robust design guidelines.

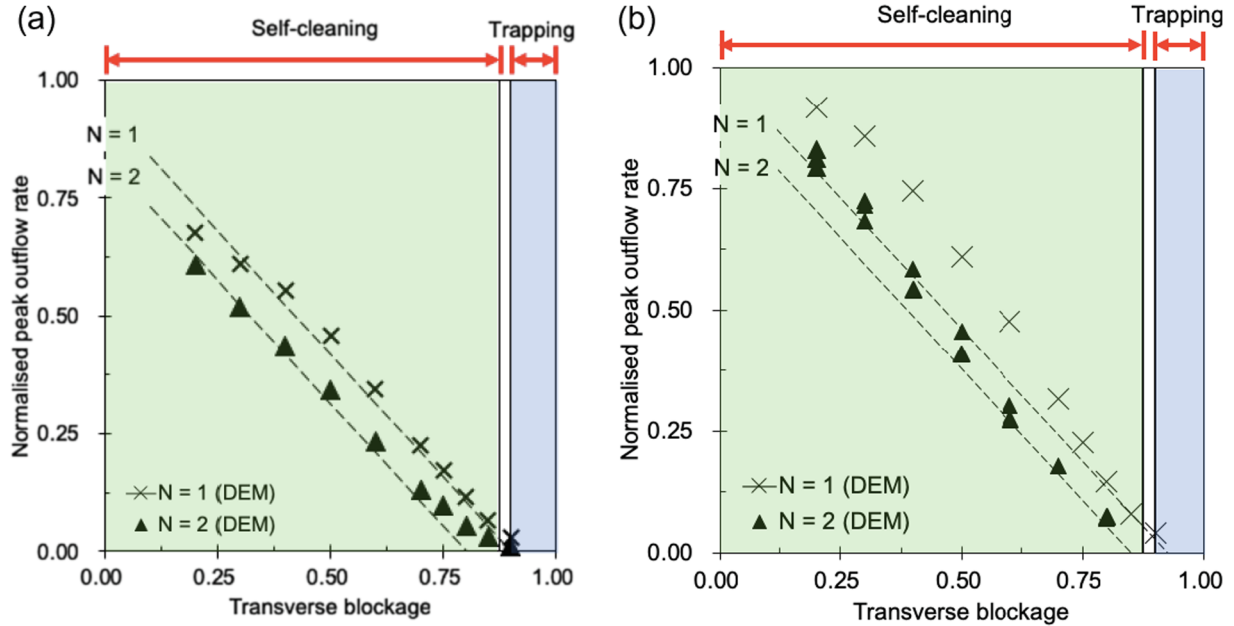


Fig. 12. Normalised peak outflow rates for various degrees of transverse blockage. (a) Channel inclination of 22°; (b) channel inclination of 30°.

## 6. Conclusions

In this study, the relationship between flow types (inviscid or frictional) and the mechanisms by which slit-structures filter out granular material were reviewed. Studies on mechanical trapping for frictional flows have thus far been limited to single-slit-structures, despite the fundamental differences caused by including multiple slits [40]. A parametric study using a calibrated DEM model was performed on frictional, monodisperse flows interacting with a slit-structure. The parameters investigated were: (i) the ratio between slit width and grain diameter  $s/\delta$ , (ii) the number of slits; (iii) the slit spacing; and (iv) the Froude number. The ratio  $s/\delta$  is related to the transverse blockage, which describes what proportion of the channel is blocked by the slit-structure.

Key conclusions are as follows:

- For slit-structures that mechanically trap grains, three regimes can be identified: (i) ‘self-cleaning’, wherein most grains pass downstream; (ii) ‘trapping’, wherein most grains become trapped; and (iii) ‘unstable’, wherein a proportion of the grains become trapped. The bounds between these regions are dictated primarily by the ratio  $s/\delta$  and the dimensionless number  $Fr$ , rather than the transverse blockage. It remains unclear whether existing designs are under- or over-conservative with regards to their intended level of trapping. Nonetheless, charts presented in this study can be used as a preliminary point for assessment.
- For a given transverse blockage, adopting dual-slit-structures rather than single-slit-structures tends to increase the trapping efficiency and decrease the peak outflow rate. This implies that multi-slit structures are a more robust choice for engineering design.
- An increase in the slit-spacing from  $2\delta$  to  $12\delta$  increases the durability of contacts for grains between slits by around 10%. This reduces the possibility of stable arches that form being broken by shearing due to outflow at the other slit. This is why for a given ratio of  $s/\delta$  and  $Fr$ , within the unstable region, the trapping efficiency is strongly influenced by the spacing of the slits. This also explains why for a given ratio of  $s/\delta$  and  $Fr$ , one slit retains more material than two, since there is no external source of shearing to keep grains passing the slit-structure downstream. This implies that adopting multiple slits spaced closely to one another are more appropriate for

controlling the flow rate without necessarily causing excessive trapping.

- Existing recommendations for slit-size design were obtained from empirical observations of inviscid flows impacting slit-structures. If these are applied to material trapped in the frictional flows considered in this study, they cover the unstable regime. Given the uncertainties in flow properties in the field, the tendency towards self-cleaning or trapping behaviour may be highly difficult to predict. Future recommendations for slit-width design should avoid this unstable regime.
- For the idealised flows in this study, the peak outflow rate varies almost linearly with the transverse blockage. For the highly-simplified flows modelled in this study, peak outflow can be estimated using an equation analogous to the Beverloo law. This equation accounts for multiple slits; the time-scale is related to the pre-impact velocity, whilst the length-scales are taken to be (i) the flow depth and (ii) the slit-opening length-scale from the original law (i.e.  $s - k_2\delta$ ). This form of the Beverloo law provides a simple way of estimating the peak outflow after designing the slit opening.

## CRediT authorship contribution statement

**G.R. Goodwin:** Conceptualization, Methodology, Software, Validation, Formal analysis, Investigation, Data curation, Writing - original draft, Writing - review & editing, Visualization. **C.E. Choi:** Conceptualization, Methodology, Resources, Writing - original draft, Writing - review & editing, Supervision, Project administration, Funding acquisition.

## Declaration of Competing Interest

The authors declare that they have no known competing financial interests or personal relationships that could have appeared to influence the work reported in this paper.

## Acknowledgements

The authors are immensely grateful for the generous financial sponsorship from the National Natural Science Foundation of China

(5170091039), as well as the Research Grants Council of Hong Kong (General Research Fund Grants 16212618; 16209717; T22-603/15N;

AoE/E-603/18).

## Appendix A. Contact model

The basic form of the Hertzian contact model implemented in LIGGGHTS [59,87] is given as follows:

$$F_{ij} = [k_n \delta n_{ij} - \gamma_n v n_{ij}] + [k_t \delta t_{ij} - \gamma_t v t_{ij}] \quad (A1)$$

where  $F_{ij}$  is contact force between  $i^{\text{th}}$  and  $j^{\text{th}}$  particles;  $k_n$  and  $k_t$  are elastic parameters corresponding to normal and tangential contacts respectively;  $\delta n_{ij}$  and  $\delta t_{ij}$  are the overlap distances for grains, corresponding to normal and tangential components respectively;  $\gamma_n$  and  $\gamma_t$  are damping constants, again corresponding to normal and tangential contacts; finally,  $v n_{ij}$  and  $v t_{ij}$  are components of the relative velocity of the two particles. Eqs. (A2a) and (A2b) give  $k_n$  and  $\gamma_n$  respectively:

$$k_n = \frac{4}{3} E^* \sqrt{r^* \delta n_{ij}} \quad (A2a)$$

$$\gamma_n = -2 \sqrt{\frac{5}{6}} \zeta(e) \sqrt{2E^*(r^* \delta n_{ij})^{1/2} m^*} \geq 0 \quad (A2b)$$

where  $\beta$  is a constant depending on the coefficient of restitution  $e$ . The variables  $r^*$ ,  $m^*$ ,  $E^*$  are given by Eqs. (A3a)–(A3c) [88], whilst  $\beta$  is given by Eq. (A3d):

$$\frac{1}{r^*} = \frac{1}{r_1} + \frac{1}{r_2} \quad (A3a)$$

$$\frac{1}{m^*} = \frac{1}{m_1} + \frac{1}{m_2} \quad (A3b)$$

$$\frac{1}{E^*} = \frac{(1 - \nu_1^2)}{E_1} + \frac{(1 - \nu_2^2)}{E_2} \quad (A3c)$$

$$\beta = \frac{\ln(e)}{\sqrt{\ln^2(e) + \pi^2}} \quad (A3d)$$

where  $\nu$  is Poisson's ratio. (Notes: for planes modelled using the DEM, the radius and mass are assumed to tend to infinity, meaning that  $r^* \rightarrow r$  and  $m^* \rightarrow m$ .)

## Appendix B. Earth-pressure calculation

Fig. B1 shows a schematic of the quantities used in Eqs. (9a) and (9b).

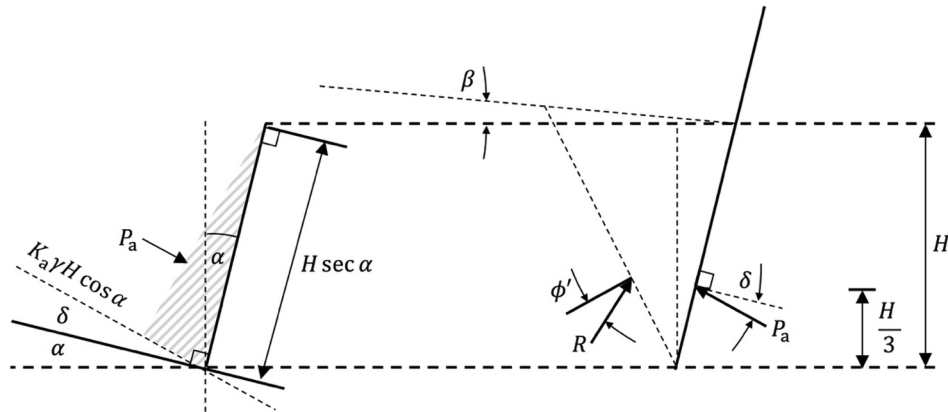


Fig. B1. Schematic of variables for active earth pressure coefficient calculation for inclined rigid wall (redrawn from [69]).

## References

- [1] Petley D. Global patterns of loss of life from landslides. *Geology* 2014;40(10):927–30.
- [2] Hungr O, Leroueil S, Picarelli L. The Varnes classification of landslide types, an update. *Landslides* 2014;11(2):167–94.
- [3] Koo RCH, Kwan JSH, Lam C, Goodwin GR, Choi CE, Ng CWW, et al. Back-analysis of geophysical flows using three-dimensional runout model. *Can Geotech J* 2018;55(8):1081–94.
- [4] Cheng D, Cui Y, Su F, Jia Y, Choi CE. The characteristics of Mocoa compound disaster event, Colombia. *Landslides* 2018;15(6):1223–32.
- [5] Cui Y, Cheng D, Choi CE, Jin W, Lie Y, Kargel JS. The Cost of rapid and haphazard urbanization: lessons learned from the freetown landslide disaster. *Landslides* 2019;16:1167–78.
- [6] Froude MJ, Petley D. Global fatal landslide occurrence from 2004 to 2016. *Nat Hazards Earth Syst Sci* 2019;18:2161–81.
- [7] Wehrmann H, Hübl J, Holzinger G. Classification of dams in torrential watersheds. In Proceedings of INTERPRAEVENT Conference 2006, Universal Academy Press, Tokyo, 2006. p. 829–38.

- [8] Toshiyuki H, Shibuya H, Katsuki S, Ishikawa N, Mizuyama T. A basic study on protective steel structures against woody debris hazards. *Int J Protect Struct* 2015;6(2):191–215.
- [9] Piton G, Recking A. Design of sediment traps with open check dams. I: hydraulic and deposition processes. *J Hydraulic Eng (ASCE)* 2016;142(2):04015045.
- [10] Piton G, Recking A. Design of sediment traps with open check dams. II: woody debris. *J Hydraulic Eng (ASCE)* 2016;142(2):04015046.
- [11] Armanini A, Larcher M. Rational criterion for designing opening of slit check dam. *J Hydraulic Eng (ASCE)* 2001;127(2):94–104.
- [12] Hübl J, Suda J, Prosek D, Kaitna R, Scheidl C. Debris flow impact estimation. Proceedings of the 11th international symposium on water management and hydraulic engineering. 2009, p. 137–48.
- [13] Armanini A. Closure relations for mobile bed flows in a wide range of slopes and concentrations. *Adv Water Resour* 2015;81:75–83.
- [14] Armanini A, Larcher M, Odorizzi M. Dynamic impact of debris flow front against a vertical wall. Proceedings of the 5th international conference on debris-flow hazards mitigation: mechanics, prediction and assessment. 2011, p. 1041–9.
- [15] Armanini A, Larcher M, Nucci E, Dumbser M. Submerged granular channel flows driven by gravity. *Adv Water Resour* 2014;63:1–10.
- [16] Choi CE, Goodwin GR, Ng CWW, Cheung DKH, Kwan JSH, Pun WK. Coarse granular flow interaction with slit-structures. *Géotechnique Lett* 2016;6:267–74.
- [17] Marchelli M, Leonardi A, Pirulli M, Scavia C. On the efficiency of slit-check dams in retaining granular flows. *Géotechnique* 2019. <https://doi.org/10.1680/jgeot.18.p.044>.
- [18] NILIM (National Institute for Land and Infrastructure Management) Manual of technical standard for establishing Sabo master plan for debris flow and driftwood, Technical Note of NILIM No. 364. Tsukuba, Japan: National Institute for Land and Infrastructure Management, Ministry of Land, Infrastructure and Transport, Japan; 2005 [In Japanese].
- [19] Ng CWW, Choi CE, Koo RCH, Goodwin GR, Song D, Kwan JSH. Dry granular flow interaction with dual-barrier systems. *Géotechnique* 2018;68(5):386–99. <https://doi.org/10.1680/jgeot.18.P.273>.
- [20] Kwan JSH. Supplementary technical guidance on design of rigid debris-resisting barriers, Technical Note No. TN 2/2012. Hong Kong, China: Geotechnical Engineering Office, Civil Engineering and Development Department, The HKSAR Government; 2012.
- [21] Iverson RM. The physics of debris flows. *Rev Geophys* 1997;35:245–96.
- [22] Armanini A, Dalri C, Larcher M. Slit-check dams for controlling debris flow and mudflow. In: Disaster mitigation of debris flows, slope failures and landslides, 2006, p. 141–8.
- [23] Fletcher L, Hungr O, Evans SG. Contrasting failure behavior of two large landslides in clay and silt. *Can Geotech J* 2002;39(1):46–62.
- [24] Sanvitale N, Bowman ET. Visualization of dominant stress-transfer mechanisms in experimental debris flows of different particle-size distribution. *Can Geotech J* 2016;54:258–69.
- [25] To K, Lai PY, Pak HK. Jamming of a granular flow in a two-dimensional hopper. *Phys Rev Lett* 2001;86(1):71–4.
- [26] Janda A, Maza D, Garcimartín A, Kolb E, Lanuza J, Clément E. Unjamming a granular hopper by vibration. *Eur Phys Lett* 2009;87:24002.
- [27] Zuriguel I, Pugnaloni LA, Garcimartín A, Maza D. Jamming during the discharge of grains from a silo described as a percolating transition. *Phys Rev E* 2003;68:030301(R).
- [28] Zuriguel I, Garcimartín A, Maza D, Pugnaloni LA, Pastor JM. Jamming during the discharge of granular matter from a silo. *Phys Rev E* 2005;71(051303).
- [29] Behringer RP. Jamming in granular materials. *CR Phys* 2015;16:10–25.
- [30] Ikeya H, Uehara S. Experimental study about the sediment control of slit Sabo dams. *J Jpn Erosion Control Eng Soc* 1980;114:37–44. [In Japanese].
- [31] Watanabe M, Mizuyama T, Uehara S. Review of debris flow countermeasure facilities. *J Jpn Erosion Control Eng Soc* 1980;115:40–5. [In Japanese].
- [32] Lien HP. Design of slit dams for controlling stony debris flows. *Int J Sedim Res* 2003;18(1):74–8.
- [33] Silva M, Costa S, Canelas RB, Pinheiro AN, Cardoso AH. Experimental and numerical study of slit-check dams. *Int J Sustain Dev Plann* 2016;11(2):107–18.
- [34] Teufelsbauer H, Wang Y, Pudasaini SP, Borja RI, Wu W. DEM simulation of impact force exerted by granular flow on rigid structures. *Acta Geotech* 2011;6:119–33.
- [35] Hákonardóttir KM, Hogg AJ, Jóhannesson T, Kern M, Tiefenbacher F. Large-scale avalanche braking mound and catching dam experiments with snow: a study of the airborne jet. *Surv Geophys* 2003;24(5–6):543–54.
- [36] Hákonardóttir KM, Hogg AJ, Jóhannesson T, Tómasson GG. A laboratory study of the retarding effects of braking mounds on snow avalanches. *J Glaciol* 2003;49(165):191–200.
- [37] Choi CE, Ng CWW, Song D, Kwan JSH, Shiu HYK, Ho KKS, et al. Flume investigation of landslide debris-resisting baffles. *Can Geotech J* 2014;51(5):540–53.
- [38] Choi CE, Ng CWW, Au-Yeung SCH, Goodwin GR. Froude characteristics of both dense granular and water flows in flume modelling. *Landslides* 2015;12(6):1197–206.
- [39] Choi CE, Ng CWW, Law RPH, Song D, Kwan JSH, Ho KKS. Computational investigation of baffle configuration on impedance of channelized debris flow. *Can Geotech J* 2015;52(2):182–97.
- [40] Zhang X, Zhang S, Yang G, Lin P, Tian Y, Wan JF, et al. Investigation of flow rate in a quasi-2D hopper with two symmetric outlets. *Phys Lett A* 2016;380:1301–5.
- [41] VanDine DF. Debris flow control structures for forest engineering. Res Br, British Columbia Ministry of Forests, Victoria, B.C., Working Paper 08/1996; 1996.
- [42] MLR (Ministry of Land and Resources) Design Standards for Debris Flow Hazard Mitigation Measures (DZ/T0239-2004). Ministry of Land and Resources of the People's Republic of China, China; 2004 [In Chinese].
- [43] SWCB (Soil and Water Conservation Bureau) Soil and water conservation handbook. Soil and Water Conservation Bureau of the Council of Agriculture, Executive Yuan and Chinese Soil and Water Conservation Society; 2005 [In Chinese].
- [44] Cui Y, Choi CE, Liu LHD, Ng CWW. Effects of particle size of mono-disperse granular flows impacting a rigid barrier. *Nat Hazards* 2018;91(3):1179–201.
- [45] Ng CWW, Choi CE, Goodwin GR. Froude characterisation for single-surge unsteady dry granular flows: impact pressure and runup height. *Can Geotech J* 2019. <https://doi.org/10.1139/cgj-2018-0529>.
- [46] Iverson RM, Logan M, LaHusen R, Berti M. The perfect debris flow? Aggregated results from 28 large-scale experiments. *JGR Earth Sci* 2010;115(F3).
- [47] Ng CWW, Choi CE, Law RPH. Longitudinal spreading of granular flow in trapezoidal channels. *Geomorphology* 2013;194:84–93.
- [48] Ashwood W, Hungr O. Estimating total resisting force in flexible barrier impacted by a granular avalanche using physical and numerical modelling. *Can Geotech J* 2016;53(10):1700–17.
- [49] Teufelsbauer H, Wang Y, Chiou MC, Wu W. Flow-obstacle-interaction in rapid granular avalanches: DEM simulation and comparison with experiment. *Granular Matter* 2009;11(4):209–20.
- [50] Salciarini D, Tamagnini C, Conversini P. Discrete element modelling of debris-avalanche impact on earthfill barriers. *Phys Chem Earth* 2010;35:172–81.
- [51] Zhao J, Shan T. Coupled CFD-DEM simulation of fluid-particle interaction in geomechanics. *Powder Technol* 2013;239:248–58.
- [52] Shan T, Zhao J. A coupled CFD-DEM analysis of granular flow impacting on water reservoir. *Acta Mech* 2014;225(8):2449–70.
- [53] Alaba A, Lambert S, Nicot F, Chareyre B. Relation between microstructure and loading applied by a granular flow to a rigid wall using DEM modelling. *Granular Matter* 2015;17(5):603–16.
- [54] Law RPH, Choi CE, Ng CWW. Discrete element investigation of the influence of granular debris flow baffles on rigid barrier impact. *Can Geotech J* 2015;53(2):179–85.
- [55] Shen W, Zhao T, Zhao J, Dai F, Zhou GGD. Quantifying the impact of dry debris flow against a rigid barrier by DEM analyses. *Eng Geol* 2018;241:86–96.
- [56] Leonardi A, Wittel FK, Mendoza M, Herrmann HJ. Lattice-Boltzmann method for geophysical plastic flows. *Recent Adv Model Landslides Debris Flows* 2015;131–40.
- [57] Leonardi A, Wittel FK, Mendoza M, Vetter R, Herrmann HJ. Particle-fluid-structure interaction for debris flow impact on flexible barriers. *Comput-Aided Civ Infrastruct Eng* 2016;31(5):323–33.
- [58] Leonardi A, Goodwin GR, Pirulli M. The force exerted by granular flows on slotted-dams. *Acta Geotech* 2019. <https://doi.org/10.1007/s11440-019-00842-6>.
- [59] Kloss C, Goniva C. LIGGGHTS – a new open source discrete element simulation software. In: Proceedings of the 5th International Conference on Discrete Element Methods, 2011, p. 25–26.
- [60] Wensrich CM, Katterfeld A. Rolling friction as a technique for modelling particle shape in DEM. *Powder Technol* 2012;217:409–17.
- [61] Bi W, Delannay R, Richard P, Taberlet N, Valance A. Two- and three-dimensional confined granular chute flows: Experimental and numerical results. *J Phys: Condens Matter* 2005;17(24):2457–80.
- [62] Kesseler M, Heller V, Turnbull B. A laboratory-numerical approach for modelling scale effects in dry granular slides. *Landslides* 2018;15:2145–59.
- [63] Jop P, Forterre Y, Pouliquen O. A constitutive law for dense granular flows. *Nature* 2006;441:727–30.
- [64] Koo RCH, Kwan JSH, Ng CWW, Lam C, Choi CE, Song D, et al. Velocity attenuation of debris flows and a new momentum-based load model for rigid barriers. *Landslides* 2016;14(2):617–29.
- [65] Faug T, Lachamp P, Naaim M. Experimental investigation on steady granular flows interacting with an obstacle down an inclined channel: study of the dead-zone upstream from the obstacle. Application to interaction between dense snow avalanches and defence structures. *Nat Hazards Earth Syst Sci* 2002;2(3–4):187–91.
- [66] Gray JMNT, Tai YC, Noelle S. Shock waves, dead-zones and particle-free regions in rapid granular free-surface flows. *J Fluid Mech* 2003;491:161–81.
- [67] Bardou E. Méthodologie de diagnostic des laves torrentielles sur un bassin versant alpin. PhD thesis, École Polytechnique Fédéral de Lausanne, 2002, 382.
- [68] Rapaport DC. The art of molecular dynamics simulation. Cambridge University Press; 2004.
- [69] CGS (Canadian Geotechnical Society). Manuel canadien d'ingénierie des fondations. 4th ed. Canadian Geotechnical Society; 2013 [In French].
- [70] Chehata D, Zenit R, Wassgren CR. Dense granular flow around an immersed cylinder. *Phys Fluids* 2003;15:1622–31.
- [71] Bharadwaj R, Wassgren C, Zenit R. The unsteady drag force on a cylinder immersed in a dilute granular flow. *Phys Fluids* 2006;18(043301).
- [72] Favier L, Daudon D, Donzé FV, Mazars J. Predicting the drag coefficient of a granular flow using the discrete element method. *J Statist Mech: Theory Exp (IoP & SISSA)* 2009;P06012.
- [73] Ng CWW, Song D, Choi CE, Liu LHD, Kwan JSH, Koo RCH, et al. Impact mechanisms of granular and viscous flows on rigid and flexible barriers. *Can Geotech J* 2016;54(2):188–206.
- [74] Wendeler C, McArdell BW, Volkwein A, Denk M. Debris flow mitigation with flexible ring net barriers – field tests and case studies. In: Monitoring, Simulation, Prevention and Remediation of Dense Debris Flows II, 2008, p. 23–31.
- [75] Campisano A, Cutore P, Modica C. Improving the evaluation of slit-check dam trapping efficiency by using a 1D unsteady flow numerical model. *J Hydraul Eng* 2014;140(7):04014024.
- [76] Castillo C, Pérez R, Gómez JA. A conceptual model of check dam hydraulics for gully control: efficiency, optimal spacing and relation with step-pools. *Hydrol Earth Syst Sci* 2014;18:1705–21.
- [77] Silva M, Costa S, Cardoso AH. Effect of plan layout on the sediment control

- efficiency of slit-check dams for stony type debris flows mitigation. *WIT Trans Ecology The Environ: River Basin Manage VIII* 2015;197:259–70.
- [78] Parsaie A, Ememgholizadeh S, Haghabi AH, Moradinejad A. Investigation of trap efficiency of retention dams. *Water Sci Technol Water Suppl* 2017;18(2):450–9.
- [79] Armanini A, Larcher M. Slit-check dams for the control of debris flow. In: 19th EGU general assembly, EGU2017, 2017, p. 12813.
- [80] Thomas CC, Durian DJ. Geometry dependence of the clogging transition in tilted hoppers. *Phys Rev E* 2013;87(5):052201.
- [81] Serrano DA, Sánchez-Silva F, Klapp J, Medina A. The Hagen-Beverloo law for outflow of granular solids from holes on side walls. *Revista Mexicana de Fisica* 2015;61:207–10.
- [82] Jóhannesson T, Gauer P, Issler D, Lied K. The design of avalanche protection dams recent practical and theoretical developments 2009. Brussels, Belgium: European Commission; 2009.
- [83] Edwards AN, Vriend NM. Size segregation in a granular bore. *Phys Rev Fluids* 2016;1:064201.
- [84] Iverson RM. Scaling and design of landslide and debris-flow experiments. *Geomorphology* 2015;244:9–20.
- [85] Aguirre MA, De Schant R, Géminard JC. Granular flow through an aperture: influence of the packing fraction. *Phys Rev E* 2014;90(012203).
- [86] Bowman ET, Take WA, Rait KL, Hann C. Physical models of rock avalanche spreading behavior with dynamic fragmentation. *Can Geotech J* 2012;49:460–76.
- [87] DCS Computing. LIGGGHTS User Manual (online) 2019, URL: <https://www.cfdem.com/media/DEM/docu/Manual.html> [Accessed on 04/04/2019].
- [88] O'Sullivan. Particulate discrete element modelling: A geomechanics perspective. CRC Press; 2011.